GAMMA-RAY BURSTS

A tera–electron volt afterglow from a narrow jet in an extremely bright gamma-ray burst

LHAASO Collaboration*†

Some gamma-ray bursts (GRBs) have a tera–electron volt (TeV) afterglow, but the early onset of this has not been observed. We report observations with the Large High Altitude Air Shower Observatory (LHAASO) of the bright GRB 221009A, which serendipitously occurred within the instrument's field of view. More than 64,000 photons >0.2 TeV were detected within the first 3000 seconds. The TeV flux began several minutes after the GRB trigger and then rose to a peak ~10 seconds later. This was followed by a decay phase, which became more rapid ~650 seconds after the peak. We interpret the emission using a model of a relativistic jet with half-opening angle of ~0.8°. This is consistent with the core of a structured jet and could explain the high isotropic energy of this GRB.

Gamma-ray bursts (GRBs) are explosions observed in distant galaxies, characterized by a rapid flash of gamma rays lasting from a fraction of a second up to several hundreds of seconds. The progenitors of long-duration ($\gtrsim$2 s) GRBs are thought to be collapsing massive stars, whereas short-duration ($\lesssim$2 s) GRBs are produced by the merger of two compact objects (*1*). The emission of a GRB consists of two stages—the prompt emission and the afterglow, which can partially overlap in time. Prompt emission has irregular variability on timescales as rapid as milliseconds, which is thought to result from internal shocks or other dissipation mechanisms that occur within the source. The afterglow emission is smoother and lasts much longer, with the flux decay usually following a power-law in time. The long-lasting afterglow is thought to result from external shocks caused by the interaction between relativistic jets (produced by the GRB) with the ambient medium at large distances from the source. The afterglow emission spans a wide range of the electromagnetic spectrum. The radio to sub-GeV emission is generally interpreted as synchrotron radiation, generated by acceleration of relativistic electrons by the external shock (*1*). The same electrons can up-scatter the synchrotron photons through the inverse Compton (IC) mechanism, producing a synchrotron self-Compton (SSC) emission component that extends to very high energy [(VHE) >100 GeV] gamma rays (*2*–*5*).

VHE emission has been detected from a few GRBs during the afterglow decay phase (*6*–*9*). However, those observations used pointed instruments that had slew to the GRB position (after it was detected by other instruments), so they did not capture the prompt emissions and rising afterglow phases. Extensive air shower detectors have a larger instantaneous field of view, have an observing duty cycle close to 100%, and do not need to be pointed, so they could potentially observe the prompt GRB and afterglow onset phases. However, attempts to observe GRBs with extensive air shower detectors have not resulted in detections (*10*–*12*).

Observations of GRB 221009A

On 9 October 2022, at 13:16:59.99 universal time (UT) (hereafter T_0), the Gamma-ray Burst Monitor (GBM) on the Fermi spacecraft detected and located the burst GRB 221009A (*13*). The Large Area Telescope (LAT) on Fermi also detected high-energy emission from the burst (*14*). The Burst Alert Telescope (BAT) on the Neil Gehrels Swift Observatory (Swift) spacecraft detected this burst when it came into view 53 min later, and Swift's X-Ray Telescope (XRT) observations began 143 s after the trigger (*15*).

The exceptionally large fluence of this event saturated almost all gamma-ray detectors during the main burst. The event fluence of GRB 221009A was measured by the Konus-Wind spacecraft from T_0 + 175 s to T_0 + 1458 s as $\gtrsim 5 \times 10^{-2}$ erg cm^{-2} in the energy range of 10 to 1000 keV (*16*), higher than any previously observed GRB. Later optical observations measured the redshift (z) of the afterglow, finding z = 0.151 (*17*, *18*). Assuming standard cosmology, the burst isotropic-equivalent energy release $E_{\gamma,\mathrm{iso}}$ is at least 3×10^{54} erg, among the highest measured.

We observed GRB 221009A with the Large High Altitude Air Shower Observatory (LHAASO). LHAASO is a VHE gamma ray extensive air shower detector (*19*), consisting of three interconnected detectors. At the time of the GBM trigger, the location of GRB 221009A was within the field of view of LHAASO at a zenith angle of 28.1° (fig. S2). We analyzed the observations of GRB 221009A with LHAASO's Water Cherenkov Detector Array (WCDA) (fig. S1) (*19*), which detected the burst at coordinates of right ascension (RA) 288.295 ± 0.005 (stat) ± 0.05 (sys) degrees and declination 19.772 ± 0.005 (stat) ± 0.05 (sys) degrees, with a statistical significance >250 standard deviations (fig. S3). Within the first ~3000 s after the trigger, WCDA detected >64,000 photons with energies between ~200 GeV and ~7 TeV associated with the GRB. It was observed by LHAASO for ~6000 s before moving out of the field of view. At these energies, another detector reported no emission ~8 hours after T_0 (*20*).

Figure 1 displays the WCDA light curve (count rate as a function of time) of GRB 221009A.

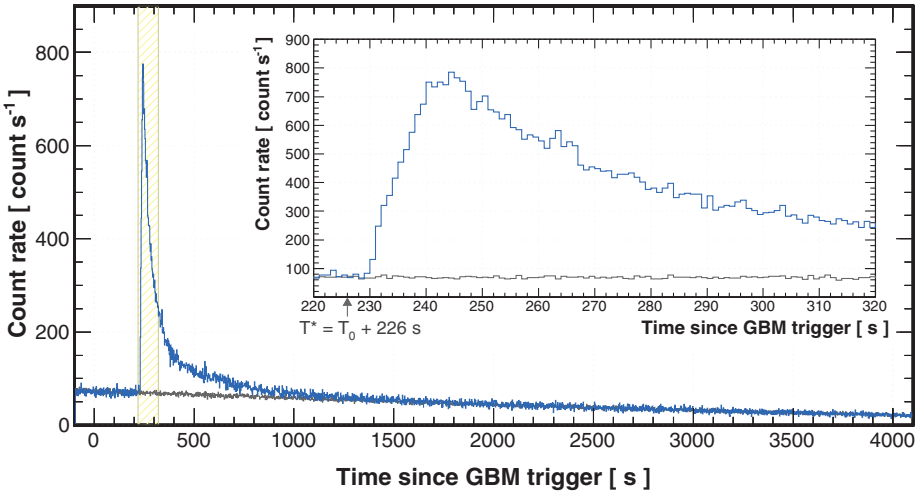

Fig. 1. Count rate light curve of GRB 221009A observed by LHAASO-WCDA. The energy range of photons observed is ~0.2 to 7 TeV. The inset panel shows a zoomed-in view of the light curve during 220 to 320 s (yellow shaded zone) after the GBM trigger (T_0), with the arrow indicating the reference time $T^* = T_0$ + 226 s for our light curve analysis (see text). Blue histograms are the data, and black histograms are the estimated background.

*Corresponding authors: X. Y. Wang (xywang@nju.edu.cn); Z. G. Yao (yaozg@ihep.ac.cn); Z. G. Dai (daizg@ustc.edu.cn); M. Zha (zham@ihep.ac.cn); Y. Huang (huangyong96@ihep.ac.cn); J. H. Zheng (mg21260020@smail.nju.edu.cn)
†LHAASO Collaboration authors and affiliations are listed in the supplementary materials.

The VHE emission exhibits a smooth temporal profile, with a rapid rise to a peak followed by a more gradual decay that persists for at least 3000 s after the peak. By contrast, the MeV gamma-ray light curves, measured by GBM (*13*) and other gamma-ray detectors (*16*, *21*), are highly variable. The GBM emission includes an initial precursor pulse lasting ~10 s, which sets T_0, followed by an extended, much brighter, and multipulsed emission episode (fig. S10). The contrast between the TeV and MeV light curves suggests that the TeV emission has a different origin than the prompt MeV emission.

Analysis of the gamma-ray data

Gamma rays emitted from distant astronomical sources are attenuated by photon interactions with the extragalactic background light (EBL). The gamma-ray spectrum that would be observed if the EBL were absent, referred to as the intrinsic spectrum, can be inferred from the observed events by correcting for EBL attenuation. We perform this correction by assuming an EBL model (*22*). Figure 2 presents both the observed and the EBL-corrected intrinsic flux spectra in the energy range from ~200 GeV to ~7 TeV, for five time intervals during which the GRB was detected by LHAASO-WCDA. The time intervals were chosen to cover the rising phase, the peak, and three periods in the decay phase. We fitted the intrinsic spectra with a power-law model (*23*), which is consistent with the data up to at least 5 TeV with no evidence for a spectral break or cut-off. The best-fitting values of the spectral indices γ of the power-law function are given in table S2. These show a mild spectral hardening in time, with γ increasing by ~0.2 between the first and last time intervals. The uncertainty in the EBL model (*22*) is equivalent to a similar change in the spectral index (table S2). During the initial main burst phase $(T_0 + [220, 230]\ \mathrm{s})$, no TeV emission is detected (significance <2.3σ), with the 95% upper limits on the flux shown in Fig. 2.

Figure 3 shows the light curve of GRB 221009A, converted to energy flux and integrated in the energy range of 0.3 to 5 TeV. The peak observed flux is $\sim 1.2 \times 10^{-5}$ erg cm^{-2} s^{-1}, which corresponds to an apparent isotropic-equivalent luminosity of $L_{\mathrm{iso,TeV}} \sim 7.3 \times 10^{50}$ erg s^{-1} in the range of 0.3 to 5 TeV, which is higher than other known sources at these energies. Because the Fermi GBM triggered on the precursor emission of this GRB, which was very weak compared with the main burst that started after a quiescent period of about 200 s (fig. S10), we set the reference time (hereafter T^*) of the afterglow light curves at the onset of the main component (*24*). Numerical studies have shown that this is a better approximation than using T_0 when investigating the afterglow emission (*24*, *25*). The first main pulse of GRB 221009A lasted from 225 to 228 s after the GBM trigger (*16*, *21*), indicating that T^* is in the range of 225 to 228 s. We measured T^* by fitting the LHAASO light curve with a model consisting of multisegment power-laws (*23*), finding $T^* = 225.7^{+2.2}_{-3.2}$ s (fig. S6). In the following analysis, we adopt $T^* = 226$ s.

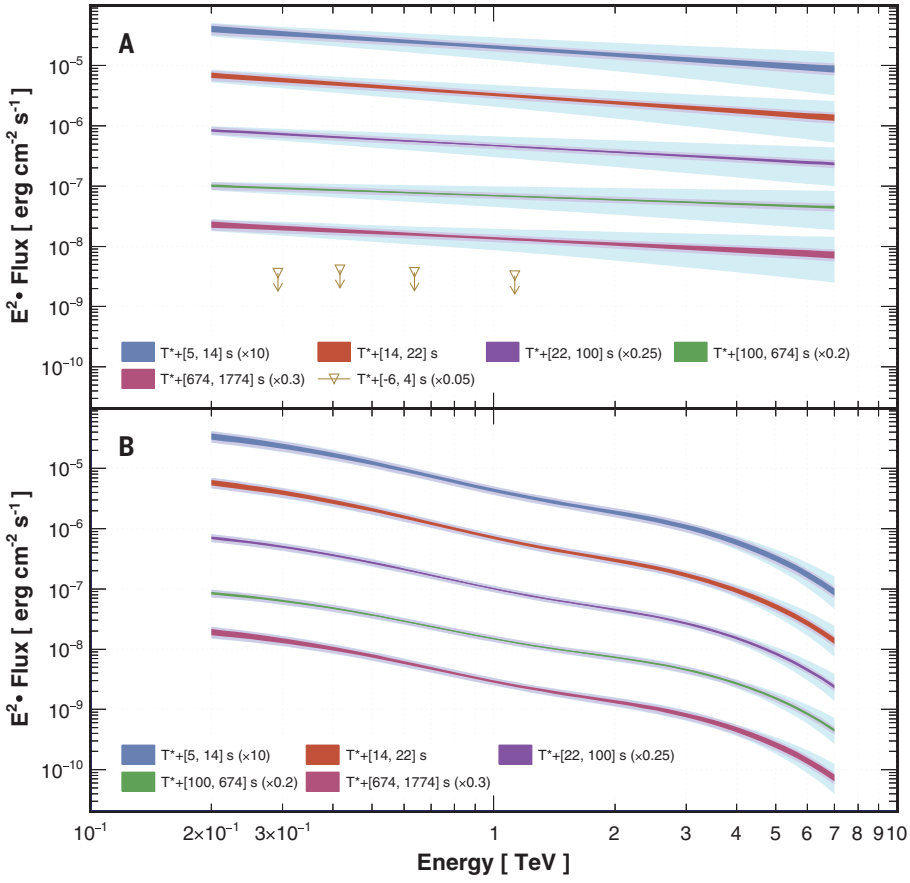

Fig. 2. Intrinsic and observed flux spectra for five time intervals. (**A**) The intrinsic spectra corrected for EBL attenuation, assuming power-law functions in the calculation (*23*). (**B**) The observed spectra obtained by reapplying the EBL attenuation to the corresponding intrinsic spectra. The shaded bands indicate 1σ ranges of statistical uncertainties (inner bands) and systematic uncertainties (outer bands). The systematic uncertainties are further divided into detector-related (middle band in light blue) and EBL-related (outer band in light cyan) components. The 95% upper limits on the intrinsic flux during the initial main burst phase $(T_0 + [220, 230]\ \mathrm{s})$ are indicated by dark orange triangles in (A). The EBL model (*22*) and its uncertainties are used to calculate the spectra and estimate the systematic uncertainties. The wave-like features in the observed spectrum are caused by the EBL attenuation at different wavelengths. An alternative calculation, independent on the EBL model, is shown in fig. S4. Goodness-of-fit tests are shown in fig. S5, and the results are listed in table S1.

Figure 3 has a four-segment shape, consisting of a rapid initial rise, a slower rise up to the peak, a slow decay after the peak, and then a steep decay after a break, each of which is consistent with a power-law function of time. We fitted the data with a semismoothed quadruple-power-law model [(SSQPL) in which a smoothed triple-power-law is connected to an initial rapid power-law rise] (*23*). We find that the slope of the rapid rise is $\alpha_0 = 14.9^{+5.7}_{-3.9}$, the slope of the slow rise is $\alpha_1 = 1.82^{+0.21}_{-0.18}$, the slope of the slow decay after the peak is $\alpha_2 = -1.115^{+0.012}_{-0.012}$, and the slope of the steep decay after the break is $\alpha_3 = -2.21^{+0.30}_{-0.83}$. The transition time from the rapid rise to the slow rise phase is $T_{b,0} = T^* + 4.85^{+0.15}_{-0.10}$ s, the peak time is $T_{\mathrm{peak}} = T^* + 18.0^{+1.2}_{-1.2}$ s, and the break time to the steep decay is $T_{\mathrm{b,2}} = T^* + 670^{+230}_{-110}$ s (table S3).

Although the rapid rise is evident in the light curve (fig. S8), the observations have insufficient temporal resolution to constrain the functional form of such a rapid rise. We assume a power-law because it is consistent with the other three segments of the light curve.

We verified that the steep decay is required by comparing the four-segment model with a three-segment model with only one segment for the whole decay phase (Fig. 3). We find that the four-segment model improves the fit over the three-segment model with a significance of

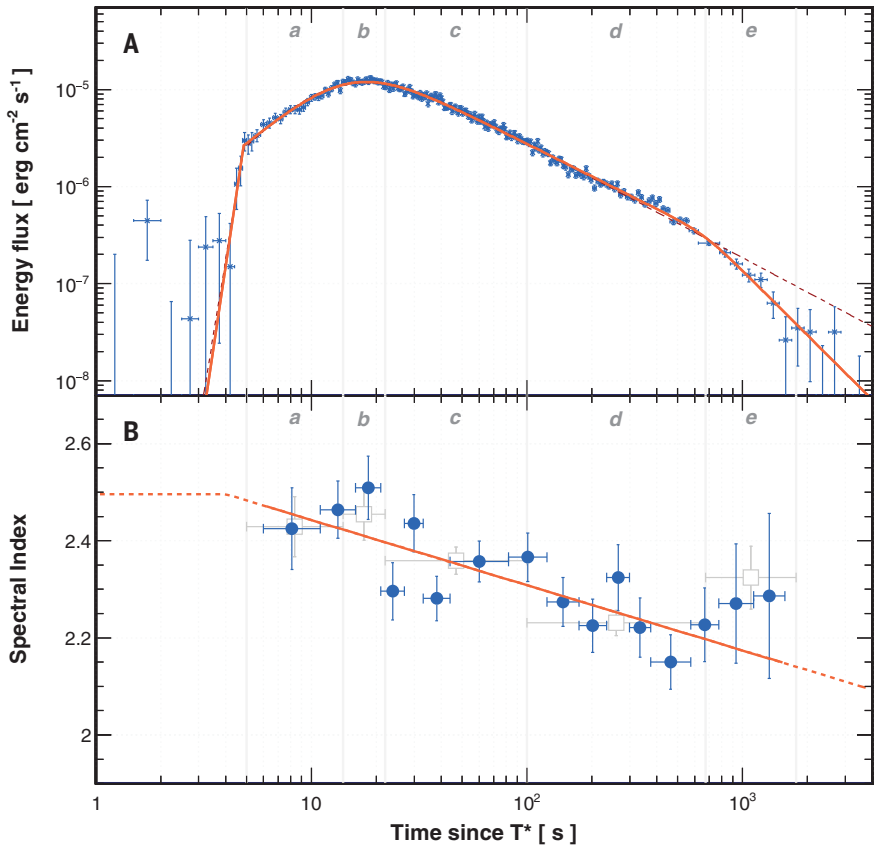

Fig. 3. Energy flux light curve and spectral evolution in the VHE band for GRB 221009A. (**A**) The light curve converted to energy flux, integrated over the energy range of 0.3 to 5 TeV. Blue points indicate the observations, with error bars indicating the ~1σ statistical uncertainty [the systematic uncertainty of ~10.7% (*23*) is not included]. The solid orange curve shows the fitted model, consisting of four joint power-laws that describe the four-segment features in the light curve: rapid rise, slow rise, slow decay, and steep decay. The dark red dashed line shows the three-segment model, which has only one segment for the entire decay phase. The best-fitting parameter values for both models are listed in table S3. (**B**) The temporal evolution of the power-law spectral index (blue circles) of photons, determined from the time-resolved intrinsic spectra. The orange line is the function $\gamma(t) = a\log(t) + b$ fitted to the data points. This model is flat before T_0 + 230 s. The time intervals for the spectrum fitting in Fig. 2 are labeled *a* to *e* in gray in both panels. The average spectral indices of these five intervals are indicated by gray hollow squares in (B).

9.2σ (*23*), indicating that a separate steep decay phase is justified by the data.

We also applied the four-segment model to light curves of sliced data samples with different energy bands (Fig. 4 and fig. S7). The best-fitting parameters are listed in table S3. The peak times for different energy bands agree with each other, within the uncertainties, without any spectral evolution, which indicates that the peak corresponds to the onset of the afterglow phase. The break in the decay phase of the light curve is observed in all energy bands. We find no systematic shift of the break time, which is also constant within the uncertainties.

We identify a small flare at $T^* + [320, 550]$ s (fig. S9). To check whether this flare affects the break at $t_{b,2}$, we masked the data during the flare period when performing the fitting. This analysis shows that the break's behavior remained the same, indicating that the flare does not affect the identification of the steep decay.

A potential systematic uncertainty in the flux arises from the adopted EBL model. To test whether the uncertainty in the EBL affects the light curve, we recalculated the light curve using the EBL intensities at the lower and upper boundaries of the EBL model (*22*). We then fitted the light curve with the same procedure, and the results are given in table S3. We find that the slopes and break times in the light curves remain almost unchanged, although the intrinsic fluxes change systematically.

Interpreting the TeV emission

TeV gamma-ray emission could be produced by relativistic electrons accelerated by internal shocks during the prompt emission (*26*) or by external shocks during the afterglow phase (*2*–*4*). The smooth temporal profile of the TeV emission in GRB 221009A suggests that it mainly results from an external shock. Synchrotron emission of relativistic electrons has a maximum energy of ≪1 TeV if the electrons are accelerated and radiate in the same zone, therefore the TeV emission of GRB 221009A is probably produced by SSC of relativistic electrons in the external shock, as has been proposed for previous TeV afterglows (*7*, *27*, *28*).

In the external shock model, the rise phase before the peak corresponds to the afterglow onset, where the forward-moving external shock sweeps up an increasing amount of ambient matter before being substantially decelerated (known as the coasting stage). The density n of the ambient matter is described by $n(R) \propto R^{-k}$, where R is the radius of the external shock, $k = 0$ corresponds to a homogeneous medium, and $k = 2$ is expected for a stellar wind from the GRB progenitor. In the homogeneous medium case, the flux increases with time as t^2 during the coasting stage, where t is the time since T^* in the observer frame, provided that the observed frequency is above the peak frequency of the SSC spectrum (i.e., in the spectral regime of $F_\nu \propto \nu^{-p/2}$, where F_ν is the flux density at frequency ν, and p is the power-law index of the electron energy distribution) (*23*). In the stellar wind case, the light curve of the TeV afterglow is expected to be flat or possibly decline with time in the same spectral regime (*23*, *29*). To produce a rising flux in the wind medium case, the Lorentz factor Γ (defined as $\Gamma \equiv 1/\sqrt{1-\beta^2}$, where β is the velocity of the shock divided by the speed of light c) of the forward shock must increase with time, perhaps as a result of energy injection. The rising slope that we observe, $\alpha_1 = 1.82^{+0.21}_{-0.18}$, is consistent with homogeneous medium without energy injection, so we infer $k = 0$. The initial rapid rise phase has a high slope, albeit with a large uncertainty. $F_\nu \propto t^4$ might apply at this stage because the spectrum is expected to be harder ($F_\nu \propto \nu^{-(p-1)/2}$) at such an early time (*23*). This phase overlaps in time with the strongest pulses of the prompt main burst emission (*16*, *21*), so energy could be transferred to the external shock by the inner ejecta, producing a rapid flux increase (*23*).

After the peak, the expected decay of the SSC emission is $t^{-(9p-10)/8}$ in the spectral regime of $F_\nu \propto \nu^{-p/2}$, when the IC scattering is in the Thomson regime (*28*). Depending on the physical parameters, the scatterings could enter into the Klein-Nishina (KN) regime, where the photon energy (in the rest frame of the scattering electron) becomes similar to the electron rest-mass energy. In the KN regime, the decay is $t^{\left(\frac{3}{2}-\frac{5p}{4}\right)}$ in the spectral regime of $F_\nu \propto \nu^{-(p-1)}$ (*23*). Both interpretations are consistent with our observed decay slope, $\alpha_2 = -1.115^{+0.012}_{-0.012}$, for $p \sim 2.1$, although the observed spectrum in this period is slightly softer than the model prediction.

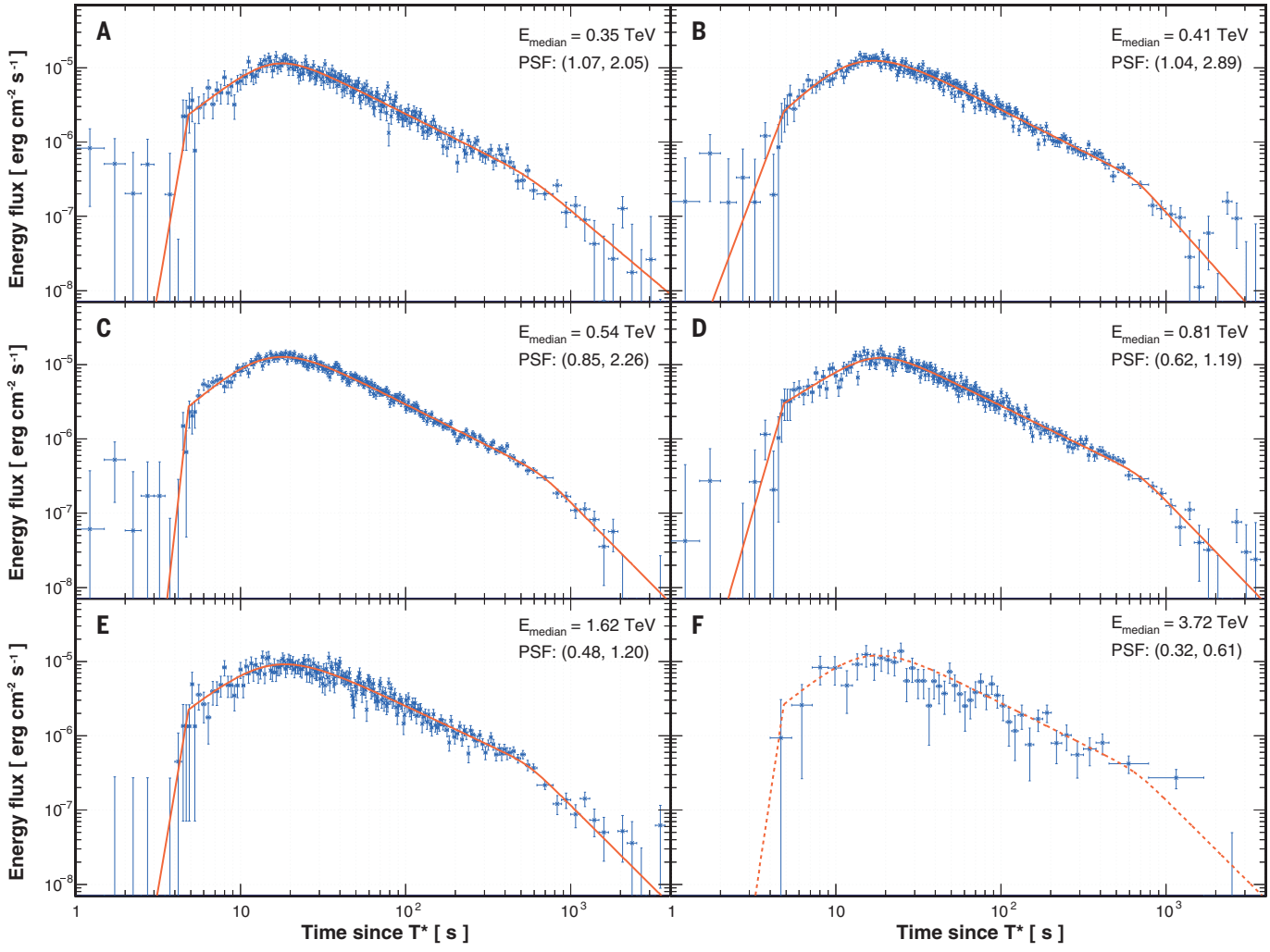

Fig. 4. Energy flux light curve in the VHE band for six N_{hit} segments. (**A** to **F**) The six segments are: [30, 33) (A), [33, 40) (B), [40, 63) (C), [63, 100) (D), [100, 250) (E), and [250, +∞) (F). The median energy (E_{median}) and point spread function (PSF) are labeled in each panel; the PSF is given as 68 and 99% containment in degrees. The orange solid lines in (A) to (E) are four-segment models fitted to the data. The overall fit in Fig. 3 is shown as the dashed line in (F) for comparison. During fitting, two parameters—the transition time from the rapid rise to the slow rise phase and the sharpness of the transition from the slow decay to the steep decay phase—were fixed to the values obtained from Fig. 3.

The light curve steepening at $t_{b,2} \simeq 670$ s after T^* cannot be a result of the KN scattering effect because the spectrum after the break does not soften. The steepening that we observe resembles a jet break, which occurs when the Lorentz factor of a GRB jet drops to $1/\theta_0$, where θ_0 is the initial half-opening angle of the jet. At this time, the jet edge becomes visible to the observer, causing a steepening in the light curve by $t^{-3/4}$ for a homogeneous medium (*30*, *31*). If the lateral expansion of the jet is fast enough (*32*–*34*), a steeper decay is expected after the jet break for the VHE emission (*23*). The early jet break of GRB 221009A implies a small θ_0, given by

$$\theta_0 \sim 0.6^\circ E_{k,55}^{-1/8} n_0^{1/8} \left(\frac{t_{b,2}}{670\ \mathrm{s}}\right)^{3/8} \quad (1)$$

where E_k is the isotropic kinetic energy of the ejecta, n is number density of the circum-burst medium, and we adopt the convention that subscript numbers x indicate normalization by a factor of 10^x in centimeter-gram-second (cgs) units. This reduces the required energy in gamma rays to $E_{\gamma,j} \equiv E_{\gamma,\mathrm{iso}}\theta_0^2/2 \sim 5.5 \times 10^{50}$ $E_{\gamma,\mathrm{iso},55}\left(\frac{\theta_0}{0.6^\circ}\right)^2$ erg for GRB 221009A. This is consistent with the typical energy reservoir of GRB jets (*35*). It has been suggested that GRBs could have a quasi-universal beaming configuration—a structured jet with high anisotropy in its angular distribution of the fireball energy about the symmetry axis (*36*, *37*). Under this assumption of a universal jet structure for GRBs, a small opening angle of GRB 221009A could imply that the brightest core of a structured jet was visible from Earth before the break, explaining the high isotropic-equivalent energy of this GRB. Combined with the low redshift of the source, the small opening angle also explains the high fluence (brightness) of this GRB.

Our identification of the TeV afterglow onset time can be used to estimate the initial bulk Lorentz factor Γ_0 of the jet. The peak time (t_{peak} ~ 18 s after T^*) of the light curve corresponds to the deceleration time, when most of the outflow energy is transferred to the shocked external medium. The initial bulk Lorentz factor is then

$$\Gamma_0 = \left(\frac{3(1+z)^3 E_k}{32\pi n m_p c^5 t_{\mathrm{peak}}^3}\right)^{1/8} = 440\, E_{k,55}^{1/8} n_0^{-1/8} \left(\frac{t_{\mathrm{peak}}}{18\ \mathrm{s}}\right)^{-3/8} \quad (2)$$

where m_p is the proton mass, and c is the speed of light. Γ_0 is almost insensitive to E_k and n. The initial Lorentz factor of GRB 221009A is consistent with the upper range of values

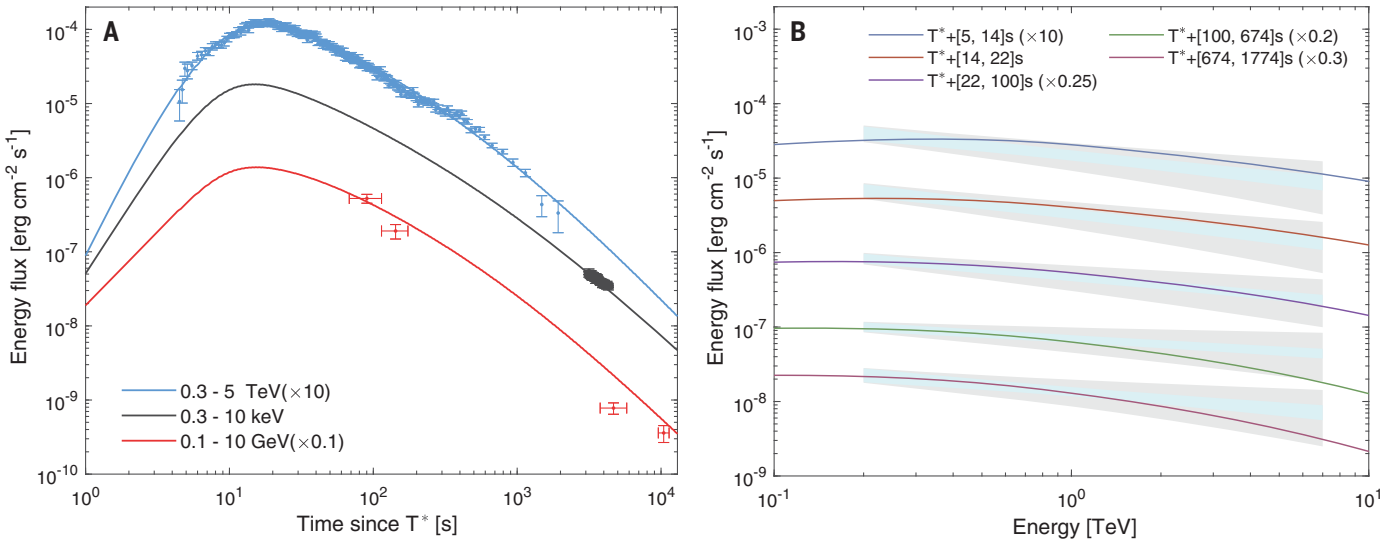

Fig. 5. Multiwavelength modeling of GRB 221009A. Data points indicate the observations, and curves are the output of the model, which assumes afterglow emission arising from external forward shocks, emitting synchrotron and SSC radiation. The adopted parameters are: $E_k = 1.5 \times 10^{55}$ erg, $\Gamma_0 = 560$, $\varepsilon_e = 0.025$, $\varepsilon_B = 6 \times 10^{-4}$, $p = 2.2$, $n = 0.4$ cm^{-3}, and $\theta_0 = 0.8°$, although these are not a unique solution (see text). (**A**) Light curves at keV (0.3 to 10 keV; black), GeV (0.1 to 10 GeV; red), and TeV (0.3 to 5 TeV; blue) energies for the first ~10^4 s after the burst. (**B**) LHAASO-WCDA spectra at five time intervals. The shaded regions indicate 1σ ranges of statistical uncertainties (inner band) and systematic uncertainties (outer bands). The five colored lines indicate the output of the model for the five time intervals.

for previous GRBs with measured Γ_0 inferred from afterglow deceleration (*38*). This implies that more energetic GRBs (in isotropic energy) have a larger initial Lorentz factor for the outflow.

Multiwavelength modeling

We performed multiwavelength modeling (*23*) of the Swift-XRT, Fermi-LAT (*39*), and LHAASO data assuming synchrotron plus SSC radiation, within the framework of our interpretation of the afterglow emission as arising from external forward shocks. We use the full KN cross section for the IC scattering and incorporate two-photon annihilation (γγ) absorption within the source (*23*). For the jet break, we consider only the geometric effect when the jet edge is seen by the observer. Because the inner core of the structured jet could be responsible for the early-time afterglow emission, we consider only the data for the first ~10^4 s after the burst. The late-time afterglow emission could, in principle, include additional contributions from the outer wider components of the structured jet (*40*, *41*).

We find a model that is consistent with the broadband light curves and the LHAASO spectra at various time intervals (Fig. 5) under the following conditions (*23*): The initial isotropic-equivalent kinetic energy of the forward shock is $E_k \sim 1.5 \times 10^{55}$ erg, and the initial bulk Lorentz factor is $\Gamma_0 \sim 560$. The electrons and magnetic field behind the shock carry fractions $\varepsilon_e \sim 0.025$ and $\varepsilon_B \sim 6 \times 10^{-4}$, respectively, of the dissipated energy of the shock. The power-law index of the electron distribution is $p \sim 2.2$, and the density of the circum-burst medium is $n \sim 0.4$ cm^{-3}. Because there is degeneracy in the parameter space, these parameters are not the only possible choice.

In this model, the x-ray afterglow is produced by synchrotron emission, and the TeV afterglow is produced by SSC emission, whereas the 0.1 to 10 GeV afterglow measured by Fermi-LAT has contributions from both synchrotron and SSC emission. We find that $\varepsilon_e > \varepsilon_B$ for the external shock, which is a necessary condition for efficient SSC radiation. The internal γγ absorption is not strong, with optical depth ≤1 for gamma rays of 5 TeV (*23*). The half-opening angle in the model is $\theta_0 \sim 0.8°$, consistent with the analytical estimate. The resulting model SSC spectrum is harder than the observed spectrum at low energy during the first two time intervals (Fig. 5B), similar to the previously studied TeV spectrum of GRB 190829A (*9*). This discrepancy between the model and observation could be a result of additional contributions to the flux measured by LHAASO-WCDA by some other emission processes, such as external IC emission.

Limit on prompt TeV emission

In the optically thin synchrotron scenario for prompt emission in GRBs (*42*, *43*), the SSC emission produced by the same population of relativistic electrons generates GeV to TeV gamma rays (*26*). Previous observations obtained only loose upper limits on the TeV flux during the prompt emission phase (*44*). GRB 221009A was observed by LHAASO during the main burst phase, yielding a differential flux limit of ~6×10^{-8} erg cm^{-2} s^{-1} at ~1 TeV from $T_0 + 220$ s to $T_0 + 230$ s (Fig. 2). Compared with the averaged MeV flux during the same period, which is 3×10^{-3} erg cm^{-2} s^{-1} [in the 20 keV to 15 MeV range; we regard this as a conservative estimate because of the saturation effect on the gamma-ray detectors (*16*)], the flux ratio between TeV and MeV emission is $R \equiv F_{\rm TeV}/F_{\rm MeV} \leq 2 \times 10^{-5}$. This is a stronger constraint than previous observations.

The internal γγ absorption suppresses the TeV flux during the prompt emission because the radius of the internal shock or dissipation is much smaller than that of the external shock. The internal dissipation radius can be estimated if we know the variability timescale of the prompt emission. Before the saturation of the GBM data, the shortest variability timescale of GRB 221009A was $t_v \sim 0.082$ s (*39*), implying that internal dissipation occurs at a distance from the source of $R_{\rm in} \sim 2\Gamma_0^2 c t_v = 10^{15}{\rm cm}(\Gamma_0/440)^2(t_v/0.082\ {\rm s})$. We estimate the optical depth for TeV emission to be $\tau_{\gamma\gamma} \sim 190(R_{\rm in}/10^{15}{\rm cm})^{-1}$ (*23*), producing strong attenuation of TeV photons, which could explain the very low flux ratio between TeV and MeV emission.

Summary and conclusions

LHAASO observed the bright GRB 221009A at the epochs covering both the prompt emission phase and the early afterglow in the TeV band, revealing the onset of afterglow emission in the TeV band. We identify a jet break in the light curve of GRB 221009A, indicating that the opening angle of GRB 221009A is ~0.8°. Under the assumption of a universal jet structure for GRBs, this implies that the orientation of

this GRB was such that the brightest core of a structured jet was visible from Earth, explaining the brightness of this GRB.

REFERENCES AND NOTES

1. P. Kumar, B. Zhang, *Phys. Rep.* **561**, 1–109 (2015).
2. R. Sari, A. A. Esin, *Astrophys. J.* **548**, 787–799 (2001).
3. X. Y. Wang, Z. G. Dai, T. Lu, *Astrophys. J.* **556**, 1010–1016 (2001).
4. B. Zhang, P. Mészáros, *Astrophys. J.* **559**, 110–122 (2001).
5. Y. C. Zou, Y. Z. Fan, T. Piran, *Mon. Not. R. Astron. Soc.* **396**, 1163–1170 (2009).
6. MAGIC Collaboration, *Nature* **575**, 455–458 (2019).
7. P. Veres *et al*., *Nature* **575**, 459–463 (2019).
8. H. Abdalla *et al*., *Nature* **575**, 464–467 (2019).
9. H.E.S.S. Collaboration, *Science* **372**, 1081–1085 (2021).
10. R. Alfaro *et al*., *Astrophys. J.* **843**, 88 (2017).
11. B. Bartoli *et al*., *Astrophys. J.* **842**, 31 (2017).
12. A. Albert *et al*., *Astrophys. J.* **936**, 126 (2022).
13. P. Veres, E. Burns, E. Bissaldi, S. Lesage, O. Roberts, "GRB 221009A: Fermi GBM detection of an extraordinarily bright GRB," GCN Circular 32636 (NASA, 2022).
14. E. Bissaldi, N. Omodei, M. Kerr, "GRB 221009A or Swift J1913.1+1946: Fermi-LAT detection," GCN Circular 32637 (NASA, 2022).
15. S. Dichiara *et al*., "Swift J1913.1+1946 a new bright hard X-ray and optical transient," GCN Circular 32632 (NASA, 2022).
16. D. Frederiks *et al*., "Konus-Wind detection of GRB 221009A," GCN Circular 32668 (NASA, 2022).
17. A. de Ugarte Postigo *et al*., "GRB 221009A: Redshift from X-shooter/VLT," GCN Circular 32648 (NASA, 2022).
18. A. J. Castro-Tirado *et al*., "GRB 221009A: 10.4m GTC spectroscopic redshift confirmation," GCN Circular 32686 (NASA, 2022).
19. X.-H. Ma *et al*., *Chinese Phys. C* **46**, 030001 (2022).
20. H. Ayala, "GRB 221009A: Upper limits from HAWC 8 hours after trigger," GCN Circular 32683 (NASA, 2022).
21. J. C. Liu *et al*., "GRB 221009A: HEBS detection," GCN Circular 32751 (NASA, 2022).
22. A. Saldana-Lopez *et al*., *Mon. Not. R. Astron. Soc.* **507**, 5144–5160 (2021).
23. Materials and methods are available as supplementary materials.
24. S. Kobayashi, B. Zhang, *Astrophys. J.* **655**, 973–979 (2007).
25. D. Lazzati, M. Begelman, *Astrophys. J.* **641**, 972–977 (2006).
26. Ž. Bošnjak, F. Daigne, G. Dubus, *Astron. Astrophys.* **498**, 677–703 (2009).
27. E. Derishev, T. Piran, *Astrophys. J. Lett.* **880**, L27 (2019).
28. X. Y. Wang, R. Y. Liu, H. M. Zhang, S. Q. Xi, B. Zhang, *Astrophys. J.* **884**, 117 (2019).
29. Y.-Z. Fan, T. Piran, R. Narayan, D.-M. Wei, *Mon. Not. R. Astron. Soc.* **384**, 1483–1501 (2008).
30. P. Mészáros, M. J. Rees, *Mon. Not. R. Astron. Soc.* **306**, L39–L43 (1999).
31. Z. G. Dai, L. J. Gou, *Astrophys. J.* **552**, 72–80 (2001).
32. J. E. Rhoads, *Astrophys. J.* **525**, 737–749 (1999).
33. R. Sari, T. Piran, J. P. Halpern, *Astrophys. J.* **519**, L17–L20 (1999).
34. Z. G. Dai, K. S. Cheng, *Astrophys. J.* **558**, L109–L112 (2001).
35. D. A. Frail *et al*., *Astrophys. J.* **562**, L55–L58 (2001).
36. E. Rossi, D. Lazzati, M. J. Rees, *Mon. Not. R. Astron. Soc.* **332**, 945–950 (2002).
37. B. Zhang, P. Mészáros, *Astrophys. J.* **571**, 876–879 (2002).
38. E.-W. Liang *et al*., *Astrophys. J.* **725**, 2209 (2010).
39. R.-Y. Liu, H.-M. Zhang, X.-Y. Wang, *Astrophys. J. Lett.* **943**, L2 (2023).
40. F. Peng, A. Königl, J. Granot, *Astrophys. J.* **626**, 966–977 (2005).
41. Y. Sato, K. Obayashi, R. Yamazaki, K. Murase, Y. Ohira, *Mon. Not. R. Astron. Soc.* **504**, 5647–5655 (2021).
42. P. Mészáros, M. J. Rees, H. Papathanassiou, *Astrophys. J.* **432**, 181 (1994).
43. Z. L. Uhm, B. Zhang, *Nat. Phys.* **10**, 351–356 (2014).
44. J. Wood, in *Proceedings of 35th International Cosmic Ray Conference (ICRC2017)*, Y.-S. Kwak, H. S. Lee, S. Oh, I. H. Park, Eds. (Proceedings of Science, 2017), p. 619.

ACKNOWLEDGMENTS

The LHAASO observatory, including its detector system, was designed and constructed by the LHAASO project team. Since its completion, it has been maintained by the LHAASO operating team. We extend our gratitude to all members of these two teams, especially those who work year-round at the LHAASO site, located more than 4400 m above sea level. Their tireless efforts ensure that the detector and all its components as well as the electricity power supply operate smoothly. **Funding:** This work was supported in China by the National Key R&D program of China under grants 2018YFA0404201, 2018YFA0404202, 2018YFA0404203, and 2018YFA0404204 and by NSFC under grants U1831208, 11833003, 12022502, 12121003, U2031105, 12005246, 12173039, 1221101008, and 12203022. Support was provided by the National SKA Program of China under grant 2020SKA0120300, the Chinese Academy of Sciences under grant YSBR-061, the Department of Science and Technology of Sichuan Province under grant 2021YFSY0030, the Natural Science Foundation of Jiangsu Province under grant BK20220757, and the Chengdu Management Committee of Tianfu New Area for research with LHAASO data. In Thailand, support was provided by the National Science and Technology Development Agency (NSTDA) and the National Research Council of Thailand (NRCT) under the High-Potential Research Team Grant Program (N42A650868). **Author contributions:** Z. G. Yao and X. Y. Wang led the data analysis and interpretation, respectively. S. C. Hu (supervised by Z. G. Yao) performed spectrum analysis. Y. Huang (supervised by C. Liu and Z. G. Yao) calculated the light curve. H. C. Li, C. Liu, and Z. G. Yao performed light curve fitting. M. Zha coordinated the entire data analysis, provided reconstruction and simulation data, and participated in spectrum analysis. H. Zhou and Zhen Wang provided cross checks. Z. G. Dai and B. Zhang contributed to theoretical interpretation and manuscript structure. H. M. Zhang performed multiwavelength data analysis and contributed to interpretation. J. H. Zheng (supervised by X. Y. Wang) modeled the multiwavelength data, and R. Y. Liu contributed to the modeling of multiwavelength data. Zhen Cao is the spokesperson of the LHAASO Collaboration and the principal investigator of the LHAASO project and coordinated the working group for this study along with the corresponding authors. Internal reviews were provided by the Physics Coordination Committee of the LHAASO Collaboration led by S. Z. Chen and the Publication Committee of the LHAASO Collaboration led by S. M. Liu and D. della Volpe. All other authors participated in data analysis, including detector calibration, data processing, event reconstruction, data quality check, and simulations, and provided comments on the manuscript. **Competing interests:** There are no competing interests to declare. **Data and materials availability:** Data and software to reproduce the results are available at https://www.nhepsdc.cn/resource/astro/lhaaso/paper.Science2023.adg9328/. This includes the observed data and detector acceptance parameters used as input for our analysis, the resulting light curve data points (shown in Figs. 1, 3, 4, and 5), spectrum data points (shown in Fig. 2 and fig. S4), the code we used for the light curve fitting, and machine-readable versions of tables S1 to S3.

SUPPLEMENTARY MATERIALS

Submitted 31 January 2023; accepted 25 May 2023
Published online 8 June 2023
10.1126/science.adg9328

A tera–electron volt afterglow from a narrow jet in an extremely bright gamma-ray burst

LHAASO Collaboration*, Zhen Cao, F. Aharonian, Q. An, Axikegu, L. X. Bai, Y. X. Bai, Y. W. Bao, D. Bastieri, X. J. Bi, Y. J. Bi, J. T. Cai, Q. Cao, W. Y. Cao, Zhe Cao, J. Chang, J. F. Chang, E. S. Chen, Liang Chen, Lin Chen, Long Chen, M. J. Chen, M. L. Chen, Q. H. Chen, S. H. Chen, S. Z. Chen, T. L. Chen, Y. Chen, H. L. Cheng, N. Cheng, Y. D. Cheng, S. W. Cui, X. H. Cui, Y. D. Cui, B. Z. Dai, H. L. Dai, Z. G. Dai, Danzengluobu, D. della Volpe, X. Q. Dong, K. K. Duan, J. H. Fan, Y. Z. Fan, J. Fang, K. Fang, C. F. Feng, L. Feng, S. H. Feng, X. T. Feng, Y. L. Feng, B. Gao, C. D. Gao, L. Q. Gao, Q. Gao, W. Gao, W. K. Gao, M. M. Ge, L. S. Geng, G. H. Gong, Q. B. Gou, M. H. Gu, F. L. Guo, X. L. Guo, Y. Q. Guo, Y. Y. Guo, Y. A. Han, H. H. He, H. N. He, J. Y. He, X. B. He, Y. He, M. Heller, Y. K. Hor, B. W. Hou, C. Hou, X. Hou, H. B. Hu, Q. Hu, S. C. Hu, D. H. Huang, T. Q. Huang, W. J. Huang, X. T. Huang, X. Y. Huang, Y. Huang, Z. C. Huang, X. L. Ji, H. Y. Jia, K. Jia, K. Jiang, X. W. Jiang, Z. J. Jiang, M. Jin, M. M. Kang, T. Ke, D. Kuleshov, K. Kurinov, B. B. Li, Cheng Li, Cong Li, D. Li, F. Li, H. B. Li, H. C. Li, H. Y. Li, J. Li, Jian Li, Jie Li, K. Li, W. L. Li, W. L. Li, X. R. Li, Xin Li, Y. Z. Li, Zhe Li, Zhuo Li, E. W. Liang, Y. F. Liang, S. J. Lin, B. Liu, C. Liu, D. Liu, H. Liu, H. D. Liu, J. Liu, J. L. Liu, J. L. Liu, J. S. Liu, J. Y. Liu, M. Y. Liu, R. Y. Liu, S. M. Liu, W. Liu, Y. Liu, Y. N. Liu, W. J. Long, R. Lu, Q. Luo, H. K. Lv, B. Q. Ma, L. L. Ma, X. H. Ma, J. R. Mao, Z. Min, W. Mitthumsiri, Y. C. Nan, Z. W. Ou, B. Y. Pang, P. Pattarakijwanich, Z. Y. Pei, M. Y. Qi, Y. Q. Qi, B. Q. Qiao, J. J. Qin, D. Ruffolo, A. Sáiz, C. Y. Shao, L. Shao, O. Shchegolev, X. D. Sheng, H. C. Song, Y. V. Stenkin, V. Stepanov, Y. Su, Q. N. Sun, X. N. Sun, Z. B. Sun, P. H. T. Tam, Z. B. Tang, W. W. Tian, C. Wang, C. B. Wang, G. W. Wang, H. G. Wang, H. H. Wang, J. C. Wang, J. S. Wang, K. Wang, L. P. Wang, L. Y. Wang, P. H. Wang, R. Wang, W. Wang, X. G. Wang, X. Y. Wang, Y. Wang, Y. D. Wang, Y. J. Wang, Z. H. Wang, Z. X. Wang, Zhen Wang, Zheng Wang, D. M. Wei, J. J. Wei, Y. J. Wei, T. Wen, C. Y. Wu, H. R. Wu, S. Wu, X. F. Wu, Y. S. Wu, S. Q. Xi, J. Xia, J. J. Xia, G. M. Xiang, D. X. Xiao, G. Xiao, G. G. Xin, Y. L. Xin, Y. Xing, Z. Xiong, D. L. Xu, R. F. Xu, R. X. Xu, L. Xue, D. H. Yan, J. Z. Yan, T. Yan, C. W. Yang, F. Yang, F. F. Yang, H. W. Yang, J. Y. Yang, L. L. Yang, M. J. Yang, R. Z. Yang, S. B. Yang, Y. H. Yao, Z. G. Yao, Y. M. Ye, L. Q. Yin, N. Yin, X. H. You, Z. Y. You, Y. H. Yu, Q. Yuan, H. Yue, H. D. Zeng, T. X. Zeng, W. Zeng, Z. K. Zeng, M. Zha, B. Zhang, B. B. Zhang, F. Zhang, H. M. Zhang, H. Y. Zhang, J. L. Zhang, L. X. Zhang, L. Zhang, P. F. Zhang, P. P. Zhang, R. Zhang, S. B. Zhang, S. R. Zhang, S. S. Zhang, X. Zhang, X. P. Zhang, Y. F. Zhang, Y. Zhang, Yong Zhang, B. Zhao, J. Zhao, L. Zhao, L. Z. Zhao, S. P. Zhao, F. Zheng, J. H. Zheng, B. Zhou, H. Zhou, J. N. Zhou, P. Zhou, R. Zhou, X. X. Zhou, C. G. Zhu, F. R. Zhu, H. Zhu, K. J. Zhu, and X. Zuo

Science **380** (6652), . DOI: 10.1126/science.adg9328

Editor's summary

Long gamma-ray bursts (GRBs) are produced by the explosion of a high-mass star, which produces a jet of material moving close to the speed of light. The LHAASO Collaboration observed the extremely bright GRB 221009A in very-high-energy (tera–electron volt) gamma rays. The GRB serendipitously occurred within the large field of view of their detector, so these data cover the rapid rise, peak emission, and gradually dimming afterglow. Modeling of the observations showed that the jet had an opening angle of less than one degree, which must have been pointed almost exactly toward Earth, explaining the unusual brightness of this GRB. —Keith T. Smith